Influence of electrochemical parameters on the characteristics of sono-electrodeposited calcium phosphate-coated carbon fiber cloth

Florian Olivier, Quentin Picard, Sandrine Delpeux Delpeux-Ouldriane, Jérôme Chancolon, Fabienne Warmont, V. Sarou-Kanian, F. Fayon, S. Bonnamy

Influence of electrochemical parameters on the characteristics of sono-electrodeposited calcium phosphate-coated carbon fiber cloth

F. Olivier[1], Q. Picard[1], S. Delpeux-Ouldriane[1], J. Chancolon[1], F. Warmont[1], V. Sarou-Kanian[2], F. Fayon[2], S. Bonnamy[1]

[1]CNRS, ICMN UMR 7374, Univ. Orléans, F-45071 Orléans, France
[2]CNRS, CEMHTI UPR 3079, Univ. Orléans, F-45071 Orléans, France

Abstract

In this work, we show that sono-electrodeposition is an efficient and versatile process for the coating of activated carbon fiber cloth (ACC) with biocompatible calcium phosphate (CaP) phases. The chemical composition, microtexture and structure of the coating were investigated by FTIR, SEM, TEM, XRD and solid-state NMR, highlighting the influence of cathodic polarization and water electrolysis on the coating characteristics. At low current density, the process leads to the formation of calcium-deficient hydroxyapatite (CDA) and octacalcium phosphate (OCP) phases with plate-like microtextures. At higher current density, the CaP coating consists of carbonated hydroxyapatite with a needle-like microtexture while, at intermediate regimes, both plate-like and needle-like microtextures are formed. The coatings were not uniform, however, for all the current density values employed, either on carbon fiber or ACC surfaces. Alternatively, it is shown that a uniform coating with a well-defined thickness can be obtained by using a constant potential value close to that of water electrolysis. In that case, the deposit consists of a homogeneous CDA phase with a plate-like nanocrystalline microtexture which exhibits a highly biomimetic structural character.

Keywords: sono-electrodeposition; coating; carbon fiber cloth; biomimetic calcium phosphates.

1. Introduction

Calcium phosphates (CaP) are well-known for their broad range of applications as biomaterials in several medical fields, especially in dentistry and orthopedic surgery [1–4]. CaP cements [5–7], CaP bioceramics [8–10] and biomimetic apatites [11,12] are among the most well-known CaPs. The choice of specific CaP-derived biomaterials depends on the targeted applications. For example, biocompatible ceramics, such as stoichiometric hydroxyapatite (HA) or biphasic calcium phosphate (BCP), are used as commercial bone substitutes [13–21]. In view of the brittleness of CaP ceramics, organic-inorganic composite CaP-derived materials such as chitosan-reinforced calcium phosphate cements [22] or apatite-collagen nanocomposites [23,24] have also been introduced to improve the mechanical properties of the device [25–31]. Among the various calcium phosphate phases used for these biomedical applications, calcium-deficient hydroxyapatite (CDA) nanoparticles exhibiting a strong biomimetic character are known to show high surface-reactivity with biological molecules and good dissolution/resorption properties [11,32–34].

Another important use of CaP materials in the orthopedic field is prosthesis coating to improve its integration in the host body [35,36]. Orthopedic prostheses are usually made of $TiAl_6V_4$ metallic alloy and *in-vivo* corrosion mechanisms can lead to the release of metallic particles or ions able to induce severe inflammatory reactions and rejection of the prosthesis [37–39]. Several processes have therefore been proposed for coating the prosthesis with a CaP layer. The most commonly used method is plasma spraying [40], but the sol-gel method [41,42], laser sputtering [43,44] or bio-mineralization [45] have also been employed. Among these techniques, electrodeposition is specifically used to perform CaP coatings on conducting metallic alloys. It consists in a controlled co-precipitation of calcium and phosphate ions on the surface of a conducting electrode. In most cases, electrodeposition is used to perform the coating of rigid metallic substrates, such as stainless steel [46], titanium [47–51], magnesium [52,53] or cobalt [39]

alloys. The major advantage of the electrodeposition process is the ability to coat porous or complex surfaces at relatively low processing temperatures in a water-based electrolyte.

More recently, devices based on carbon materials have been developed to offer new perspectives in the field of orthopedic applications [31,54–57]. In order to improve the biological properties of the activated carbon fiber cloth (ACC) involved in such devices, Han *et al.* [58–60] proposed to coat the ACC surface with a biocompatible CaP layer using sono-electrochemical deposition at a constant current density (20 mA/cm²), in order to take advantage of the electrical conducting properties of ACC. In their work, they pointed out that the CaP-coating significantly improved the *in vitro* biocompatibility with human osteoblasts when compared with pristine ACC [58,59]. They also reported a significant influence of experimental conditions, such as sonication [58] and electrolyte concentration [60], on the morphology and the chemical composition of the CaP coatings. However, the influence of electrochemical parameters, such as the type of cathodic polarization, on the precise microtexture (TEM) and structure (XRD and solid-state NMR) of CaP coatings remain to be elucidated.

In this study we therefore investigated in detail the effect of electrochemical parameters, such as applied current density or electrical potential value, not only on the CaP composition and morphology but above all on the coating uniformity, the chemical homogeneity, microtexture and structure of the CaP coatings using a broad range of characterization techniques (FTIR, SEM, TEM, XRD and solid-state NMR).

2. Experimental

2.1. Substrate

The material substrate consists of an activated carbon fiber cloth (ACC) obtained by the weaving of carbon fibers further physically activated with water vapor. It is referenced KIP 1200

(Dacarb®, France). Prior to use, the ACC, 40 mm*30 mm* 0.5 mm in size, was washed with boiling distilled water using a Soxhlet® extractor to remove any traces of contaminants coming from the activation and carbonization steps. After 12 hours of washing, the ACC was dried under vacuum at 70 °C.

2.2. Synthesis of the CaP coatings

CaP coating on the ACC was performed at room temperature using sono-electrochemical deposition. The electrolyte consisted of a mixture of calcium nitrate tetrahydrate $Ca(NO_3)_2$, $4H_2O$ (Sigma-Aldrich, BioXtra, purity 99.0%), and ammonium dihydrogenophosphate $NH_4H_2PO_4$ (Alfa Aesar, purity 98.0%), maintaining a Ca/P ratio of 1.67 with $[Ca^{2+}]$ = 5 mmol/L. The initial pH was kept at 4.8. An electrochemical cell was home-made to use ACC as the working electrode, a platinum basket surrounding the ACC was used as the counter electrode and Hg/Hg_2SO_4 (Radiometer analytical, France) was used as the reference electrode. The cathodic polarization of the carbon electrode was performed using a potentiostat/galvanostat (Biologic Science Instruments VMP-2, France) with current densities tested in a wide range from 25 to 270 mA/g for 6 hours. Cathodic polarization was also performed with a constant potential of -1 V/Hg/Hg_2SO_4, which is the theoretical barrier potential of water reduction at initial pH (= 4.8). Sonication (35 kHz, 30%) was applied during polarization (ultrasonic bath, Transsonic Ti-H-10, Fisher Scientific France).

2.3. Characterization techniques

The characteristics of the ACC substrate (ACC) were analyzed. Elemental analysis (weight %) of C and O was determined using a Flash 2000 (CHON-S) analyzer (Thermo Scientific France). The porosity was characterized by N_2 and CO_2 adsorption respectively at 77 K and 273 K, using an Autosorb-1 (Quantachrome). The total pore volume was estimated from the amount adsorbed at P/P0 = 0.95. The micropore (pore size < 2 nm) and mesopore (2 nm < pore size < 50 nm) volumes

were determined by applying the density functional theory (DFT) method to the N_2 isotherms assuming a slit pore shape. The Dubinin–Radushkevich (DR) theory was applied to the CO_2 adsorption isotherm at 0 °C to estimate the volume of ultramicropores (pore size < 0.7 nm). The pK_A distribution of functional groups grafted on the ACC surface and the pH_{PZC} (pH value corresponding to an ACC net charge of zero) were measured by potentiometric titration with NaOH (0.1 mol/L) using a very low incremental volume (0.01 ml) in a wide range of pH = 3-11.

Characterizations of the morphology, microtexture, chemical composition and structure of the CaP coatings were performed. The CaP coating morphology and thickness were investigated by scanning electron microscopy (SEM-Hitachi S4500) operating at 5 kV. To determine the microtexture of CaP coatings, transmission electron microscopy (TEM) images were acquired with a TEM-PHILIPS CM20 operating at 200 kV. For sample preparation, 1 mg of coating was scraped from the carbon surface, dispersed in ethanol and sonicated for 30 sec; a droplet of the suspension was deposited on an amorphous carbon coated copper grid (Electron Microscopy Sciences). TEM-Energy dispersive X-ray spectroscopy (EDS) analysis (EDAX detector, Eindhoven, The Netherlands) was performed using a probe size of about 100 - 150 nm to determine the Ca/P atomic ratios from the Ca peak (K_α Ca = 3.691 keV) and P peak (K_α P = 2.015 keV) of the TEM-EDS spectrum. The crystallographic structure of the CaP coatings was analyzed by X-Ray diffraction (XRD) using an INEL diffractometer (CSP120, France), working at 40 kV and 30 mA (K_α Cu = 1.5418978 Å) with a curve detector (angular instrumental resolution of 0.05°), in the range 2θ = 10° – 80°, in transmission mode, using an Si (111) monochromator. Fourier transform infrared spectroscopy (FTIR) spectra were acquired on KBr pellets in transmission mode using a Nicolet 6700 spectrometer in the range 4000-400 cm^{-1} (resolution = 4 cm^{-1}, 256 scans). Pellets were prepared by admixing 1 mg of CaP sample (with ACC) with 99 mg of KBr. Solid-state nuclear magnetic resonance (NMR) experiments were performed using a Bruker Avance I spectrometer

operating at a magnetic field of 7.0 T (^{1}H and ^{31}P Larmor frequencies of 300.13 MHz and 121.50 MHz, respectively), equipped with a 4 mm magic-angle spinning (MAS) NMR probehead. The ^{31}P 1D quantitative MAS, {^{1}H}-^{31}P cross-polarization (CP) MAS and 2D {^{1}H}-^{31}P heteronuclear correlation spectra were recorded at a sample spinning frequency of 10 kHz. ^{1}H and ^{31}P NMR chemical shifts were referenced to TMS and H_3PO_4 in solution (85%), respectively.

3. Results and discussion

3.1. Characterization of the ACC substrate

The chemical and textural characteristics of KIP 1200 ACC are given in Table 1. The data obtained from elemental analysis show that the ACC substrate contains 92.4 wt% of carbon and 1.6 wt% of oxygen. The potentiometric titration indicates that KIP 1200 ACC pH_{PZC} is basic (9.4) and that it presents a low amount of acidic functional groups (0.48), leading to a rather hydrophobic surface.

Table 1
Chemical and textural characteristics of KIP 1200 ACC substrate. **(2-column fitting image)**

Elemental analysis (mass.%)		**pKa distribution (mmol/g)**			**N_2 and CO_2 adsorption**				
% C	% O	pH_{PZC}	3<pKa<7	7<pKa<11	Acidic functional groups	Vmicro[1] N_2, DFT cm^3/g	Vmeso[1] N_2, DFT cm^3/g	Vultramicro[2] CO_2, DR cm^3/g	Vtotal cm^3/g
92.4	1.6	9.4	0.05	0.43	0.48	0.51	0.09	0.52	0.68

[1]The microporous and mesoporous volumes were determined by applying the density functional theory (DFT) method to the N_2 adsorption isotherms.
[2] The ultramicroporous volume was determined by applying the Dubinin-Radushkevich (DR) theory to the CO_2 adsorption isotherm.

SEM images show that the ACC substrate is made of woven carbon fibers. Their diameters are in the 10-12 µm range and micropores are assumed to be directly accessible all along the fibers (Fig. 1 (a)).

As obtained from the gas adsorption characterization, KIP 1200 ACC exhibits a high BET surface area (1693 m^2/g). It presents a narrow pore size distribution and it is almost exclusively

microporous with a negligible amount of mesopores (Table 1 and Fig. 1 (b)). The mesoporous volume represents 13% of the total pore volume, and among the micropores (0.7 < pore size < 2 nm) the ultramicroporous volume (pores narrower than 0.7 nm) represents about 76% of the total pore volume.

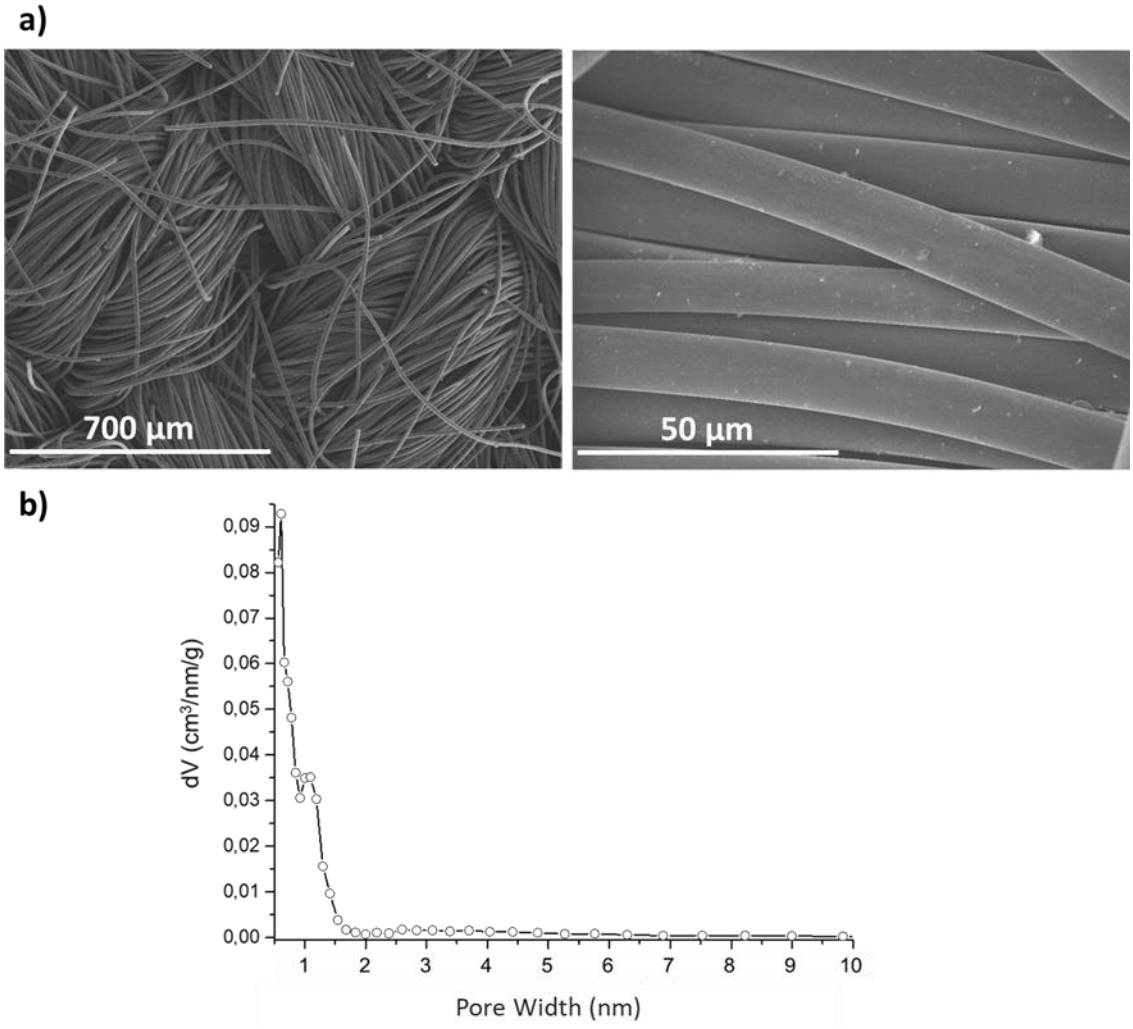

Fig. 1. a) SEM micrographs of pristine KIP 1200 ACC substrate made of woven carbon fibers 10-12 µm in diameter and b) Pore size distribution of KIP 1200 ACC substrate (N_2 adsorption at 77 K). **(2-column fitting image)**

3.2. Uniformity and mass uptake of CaP deposits

ACC substrate surfaces were observed before (Fig. 2 (a)) and after sono-electrodeposition experiments at different current densities, i.e. 25 mA/g (Fig. 2 (b)), 75 mA/g (Fig. 2 (c)), 270 mA/g

(Fig. 2 (d)) and for a -1 V constant potential (Fig. 2 (e)). Whatever the current density, a non-uniform CaP coating with uneven thickness was observed. On the contrary, at constant potential a uniform CaP coating was deposited on the ACC surface.

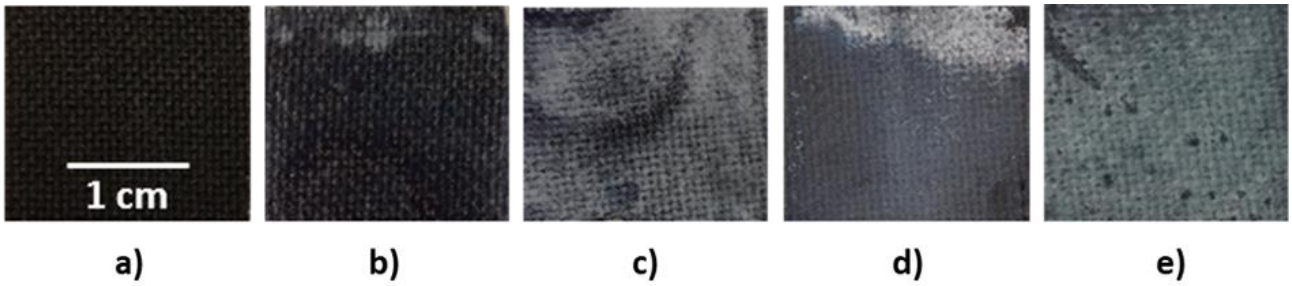

Fig. 2. Photographs of a) pristine KIP 1200 ACC; b) to d) different CaP coatings on ACC substrate observed at different current densities: b) 25 mA/g , c) 75 mA/g, d) 270 mA/g and e) experiment performed at a -1 V constant potential. **(2-column fitting image)**

Fig. 3 illustrates the mass uptake of CaP/ACC materials as a function of the cathodic polarization. For CaP coatings performed at a constant current, the mass uptake increases from 2 to 10 wt% with the current increase. When the CaP mass uptake obtained at -1 V constant potential is plotted on the curve, it is close to 60 mA/g current density. It should be noted that, in such experimental conditions, a much lower standard deviation is obtained, indicating a better control of the sono-electrodeposition process.

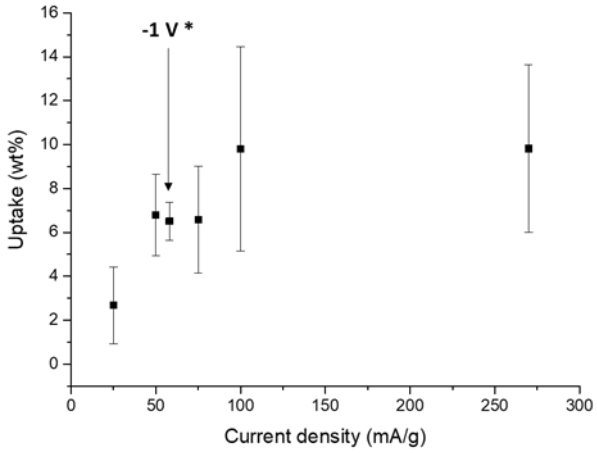

Fig. 3. Variation of the CaP mass uptakes as a function of the cathodic polarization applied. Error bars were determined statistically by taking into account five experiments. **During the constant potential (-1 V) application, a constant current density close to 60 mA/g was measured. **(1-column fitting image)**

3.3. Morphology and thickness of CaP coatings

SEM micrographs illustrating the CaP coatings synthesized at different cathodic polarizations are depicted in Fig. 4. It clearly shows that different coating morphologies can be obtained with the sono-electrodeposition process: low current densities (25 and 50 mA/g) and constant potential (-1 V) lead to a plate-like morphology, while intermediate (75 mA/g) and high current densities (100 and 270 mA/g) lead to the formation of aggregates. Plate-like particles and aggregates do not form bridges between fibers, maintaining the flexibility of the ACC substrate.

From high magnification SEM images, the CaP coating thickness (t) was determined by measurement on fiber cross-sections or on coating fractures (Fig. 5). It is respectively: $t < 0.1$ µm at 25 mA/g current density; $t < 0.1$ µm at 50 mA/g current density; $0.25 < t < 0.6$ µm at 75 mA/g current density; $0.6 < t < 2$ µm at 270 mA/g current density; and $1.3 < t < 1.7$ µm at -1 V constant potential. Thus, an increase in current density from 25 to 270 mA/g leads to an increase in CaP coating thickness from less than 0.1 µm to 2 µm. At -1 V constant potential, the CaP coating is uniformly spread and a 1.5 µm thickness maintains the flexibility of the carbon cloth.

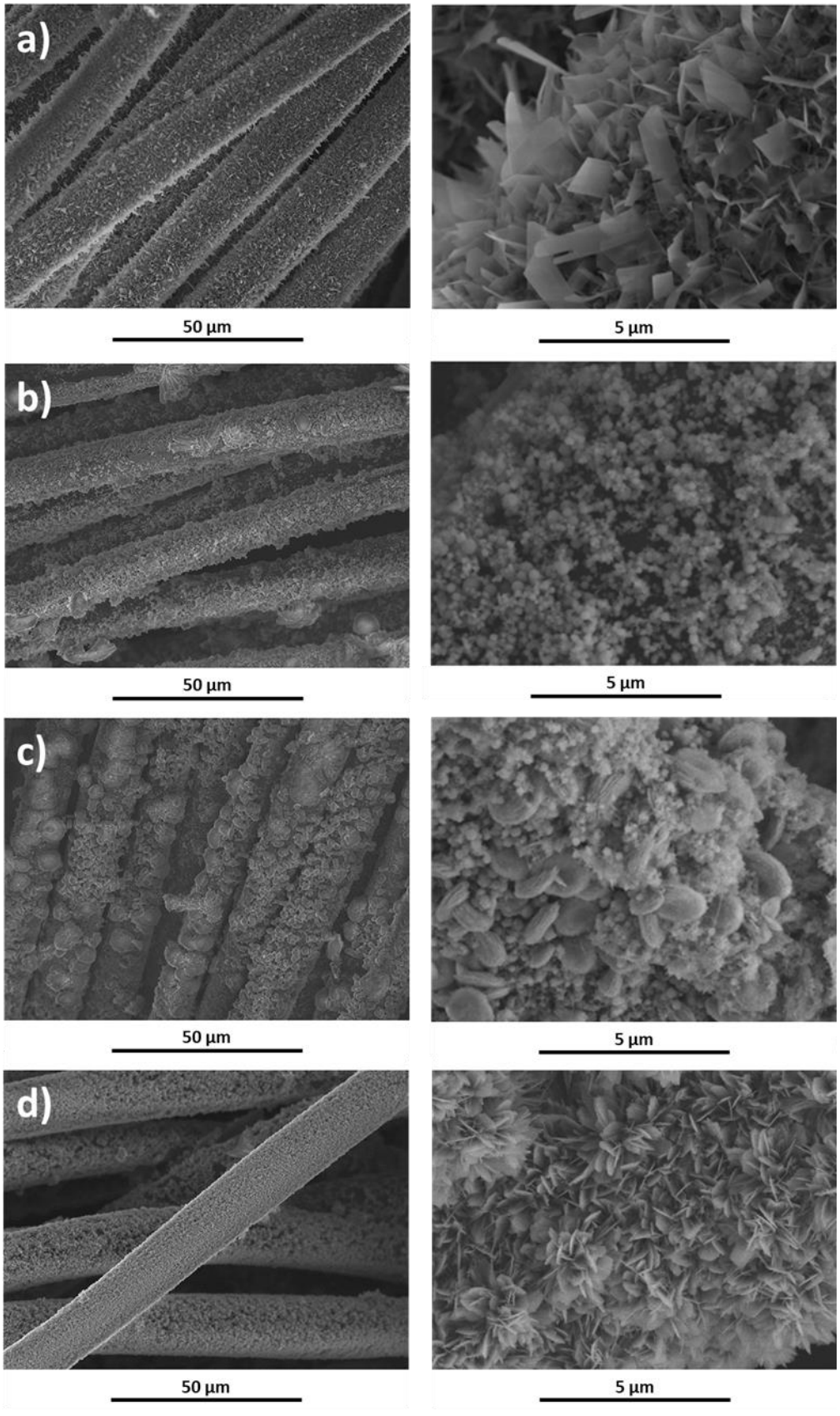
a)
50 µm
5 µm
b)
50 µm
5 µm
c)
50 µm
5 µm
d)
50 µm
5 µm

Fig. 4. SEM micrographs of CaP coatings synthesized under different cathodic polarizations: a) 25 mA/g, b) 75 mA/g, c) 270 mA/g and d) -1 V**. (2-column fitting image)**

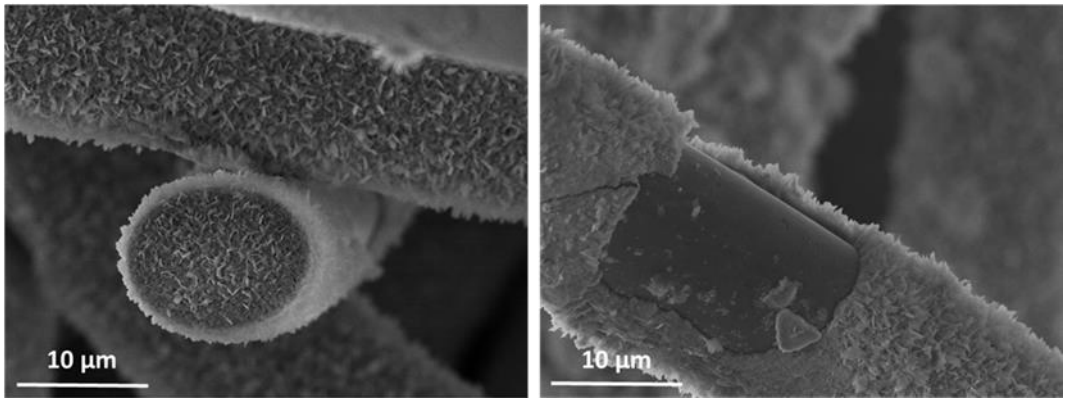

Fig. 5. Examples of SEM micrographs used to measure the thickness of CaP coatings deposited on carbon fibers.

3.4. Microtexture and Ca/P ratio

TEM characterization was used to define and describe the SEM morphologies (plate-like and aggregate-like). Three kinds of microtexture are observed, depending on the cathodic polarization (Fig. 6): nanocrystallites with a plate-like microtexture at 25 mA/g (Fig. 6 (a)) and -1 V (Fig. 6 (d)); a needle-like microtexture at 270 mA/g (Fig. 6 (c)); and a mixture of these two microtextures at 75 mA/g (Fig. 6 (b)). Due to the thinness of CaP plate-like nanocrystallites, a folding of their edges is often observed (Fig. 6 (a) and (d)). Needles are several 100 nm in length and less than 50 nm in width (Fig. 6 (c)).

The Ca/P ratios are: Ca/P = 1.40 ± 0.08 at 25 mA/g current density; Ca/P = 1.44 ± 0.04 at 50 mA/g current density; Ca/P = 1.68 ± 0.14 at 75 mA/g current density; Ca/P = 1.62 ± 0.11 at 100 mA/g current density; Ca/P = 1.71 ± 0.08 and Ca/P = 2.3 ± 0.3 at 270 mA/g current density; and Ca/P = 1.4 ± 0.1 at -1 V constant potential (Fig. 6 (e)). At 25 mA/g, the measured Ca/P ratio (1.40 ± 0.08) is close to that of octacalcium phosphate (OCP, Ca/P = 1.33) and a plate-like morphology is observed (Fig. 6 (a)). From 75 to 270 mA/g, Ca/P ratios are close to that of hydroxyapatite (HA, 1.67) and a needle-like morphology is observed (Fig. 6 (b) and (c)). CaP ratios ranging between

these two values were measured when using a 50 mA/g current density or for a -1 V constant potential, suggesting that the CaP coatings formed under these conditions could be a calcium-deficient hydroxyapatite (CDA) phase or a mixture of OCP and HA. At 270 mA/g, two distinct Ca/P ratios (1.71 ± 0.08 and 2.3 ± 0.3) were obtained; the higher one results from a mixture of HA and calcite ($CaCO_3$) phases, as was confirmed by XRD (Fig. 8).

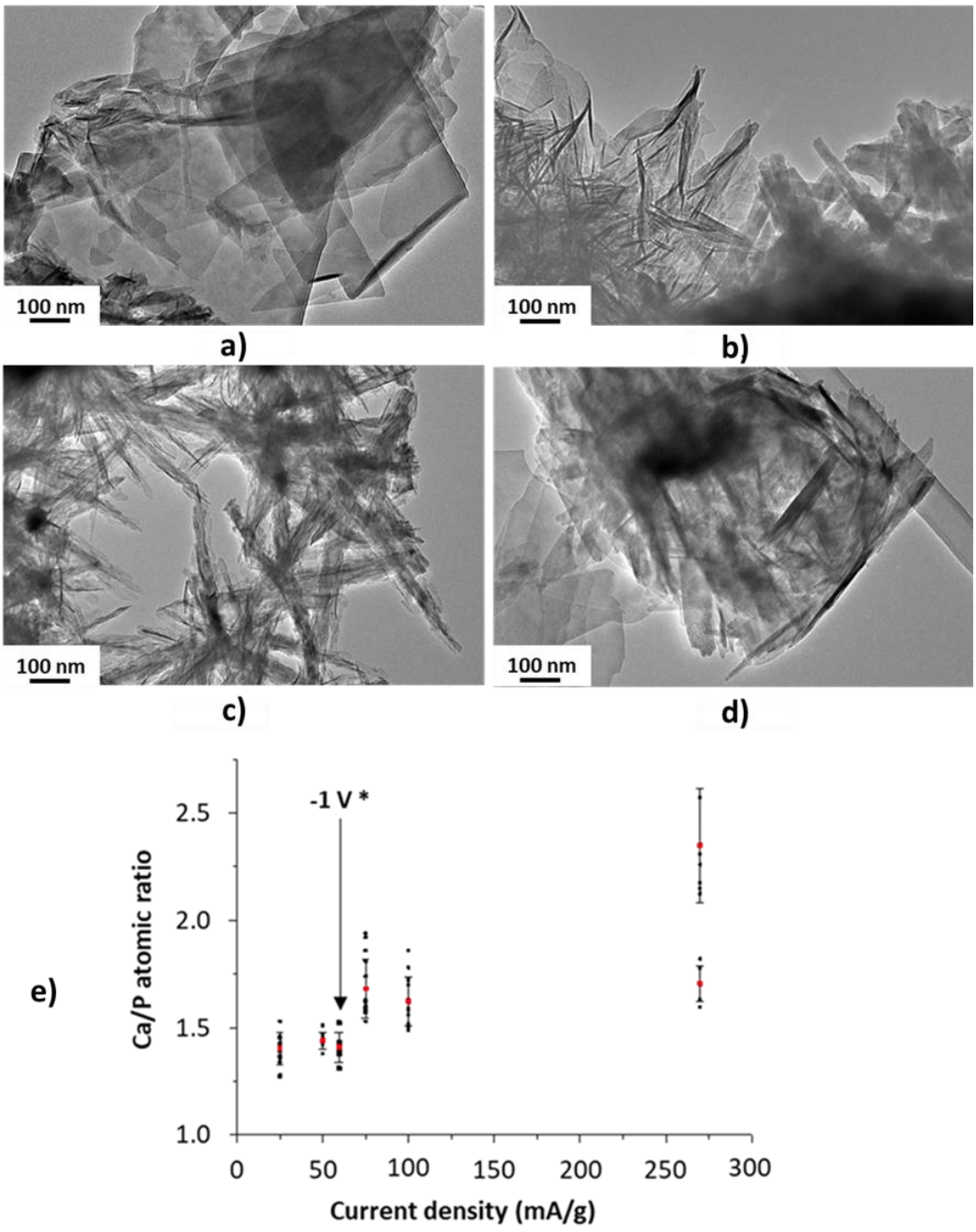

Fig. 6. From a) to d) TEM micrographs of different CaP coatings synthesized under different cathodic polarizations: a) 25 mA/g, b) 75 mA/g, c) 270 mA/g and d) -1 V; e) Ca/P atomic ratio obtained from TEM-EDS analysis as a function of the cathodic polarization. *During the constant potential (-1 V) application, a constant current density close to 60 mA/g was measured. **(2-column fitting image)**

3.5. Crystallographic structure of CaP/ACC materials

Fig. 7 shows the needle-like and plate-like microtextures observed at high magnification in TEM, associated with their selected area electron diffraction (SAED) patterns. The SAED pattern of the needles (Fig. 7 (a), 270 mA/g) shows well-defined Bragg reflections attributed to (002), (211), (112), (300) and (004) reflections of hexagonal HA structure (JCPDS n°74-0566) with $P6_3/m$ space group symmetry. The occurrence of arcs for (002) reflections is related to a preferred direction for the HA crystal growth along the c-axis of the hexagonal structure. The plate-like microtexture formed at low current density (25 mA/g) or at constant potential (-1 V) consists of nanocrystallites with a lamellar organization (Fig. 7 (b) and (c), respectively). SAED patterns show an intense ring with some Bragg reflections that can be assigned to (211), (112) and (300) reflections of HA (JCPDS n°74-0566) or of CDA. Weaker intensity Bragg peaks can also be assigned to (002) and (004) reflections of HA/CDA. However, the presence of other CaP phases with similar reflections such as OCP cannot be excluded on this basis.

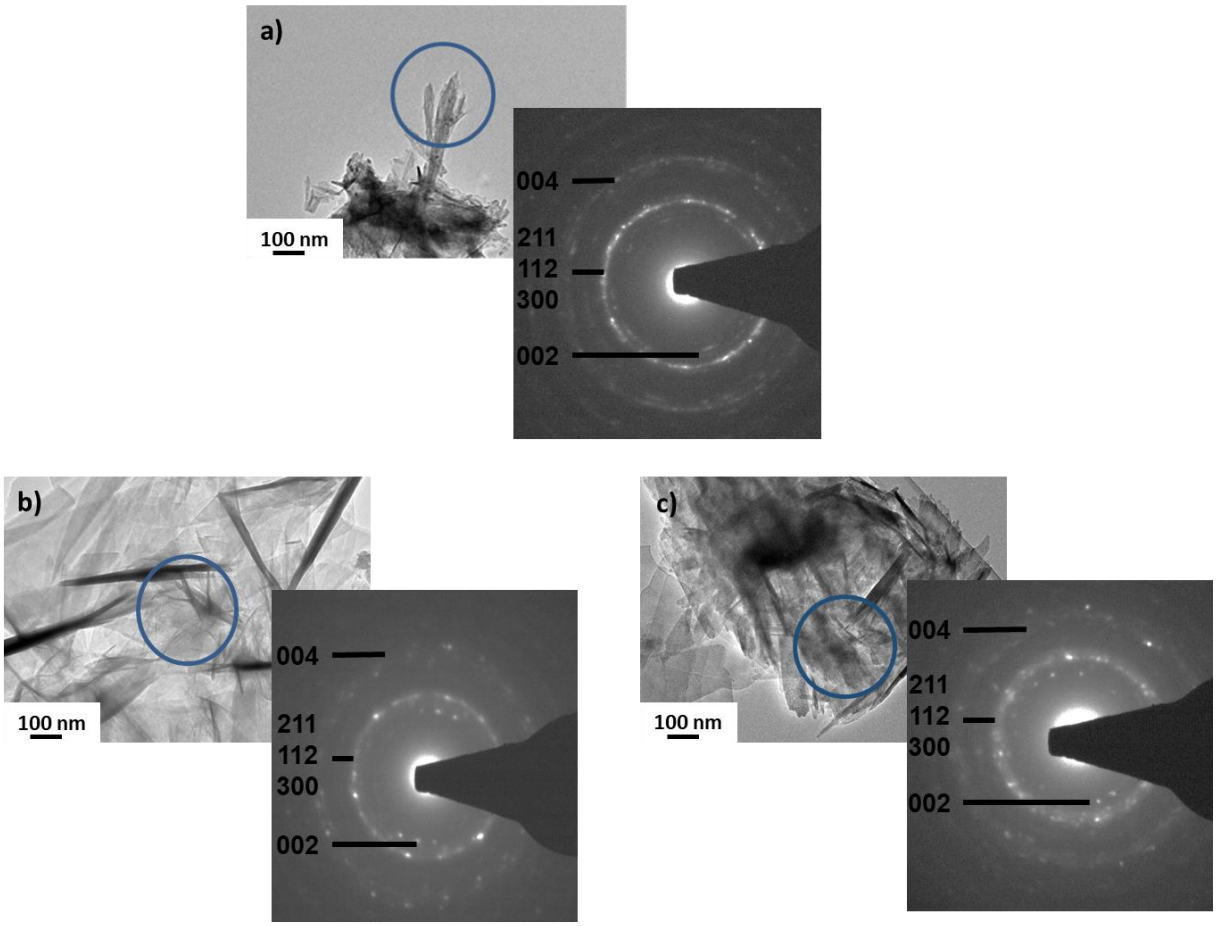

Fig. 7. TEM micrographs and their SAED patterns for coatings formed at: a) 270 mA/g, b) 25 mA/g and c) -1 V**. (2-column fitting image)**

As expected, the XRD diffractograms of CaP coatings obtained from 50 to 270 mA/g current density (Fig. 8 (a)) show intense diffraction peaks located at 2θ = 25.9°, 32° and 32.9° corresponding to (002), (211) and (300) reflections of HA (JCPDS n°74-0566). The peaks are relatively broad which could be due to the nanometric size of coherent diffraction domains, or to a structural disorder related to the partial substitution of phosphate and hydroxyl ions by carbonate ions in the HA structure, or to both phenomena. A similar diffractogram is obtained for a CaP coating deposited at -1 V potential constant (Fig. 8 (c)). It is only for a current density of 270 mA/g that additional peaks characteristic of the allotropic form of $CaCO_3$ (JCPDS n°05-0586) are observed at 2θ = 29.4° 36.0° and 39.4°. In contrast, the diffractogram of the CaP coating obtained

at 25 mA/g (Fig. 8 (b)) exhibits peaks at 2θ = 9.42°, 9.80° and 24.32° characteristic of OCP (respectively (200), (010) and (321) reflections (JCPDS n°79-0423). Additional peaks at 2θ = 32° and 32.9° also reveal the presence of an HA or a CDA phase ((211) and (300) reflections), in addition to OCP. Note that for CaP coatings formed at 25 mA/g and -1 V (Fig. 8 (b) and (c)) with plate-like morphologies, diffractograms were directly recorded on the ACC/CaP materials (i.e. without scraping the ACC substrate). The reason is that at 25 mA/g, the low CaP uptake and small thickness did not enable a sufficient quantity of CaP coating to be collected, whereas at -1 V, the high adherence between the CaP coating and the ACC substrate makes it difficult to collect only the CaP coating without carbon fibers.

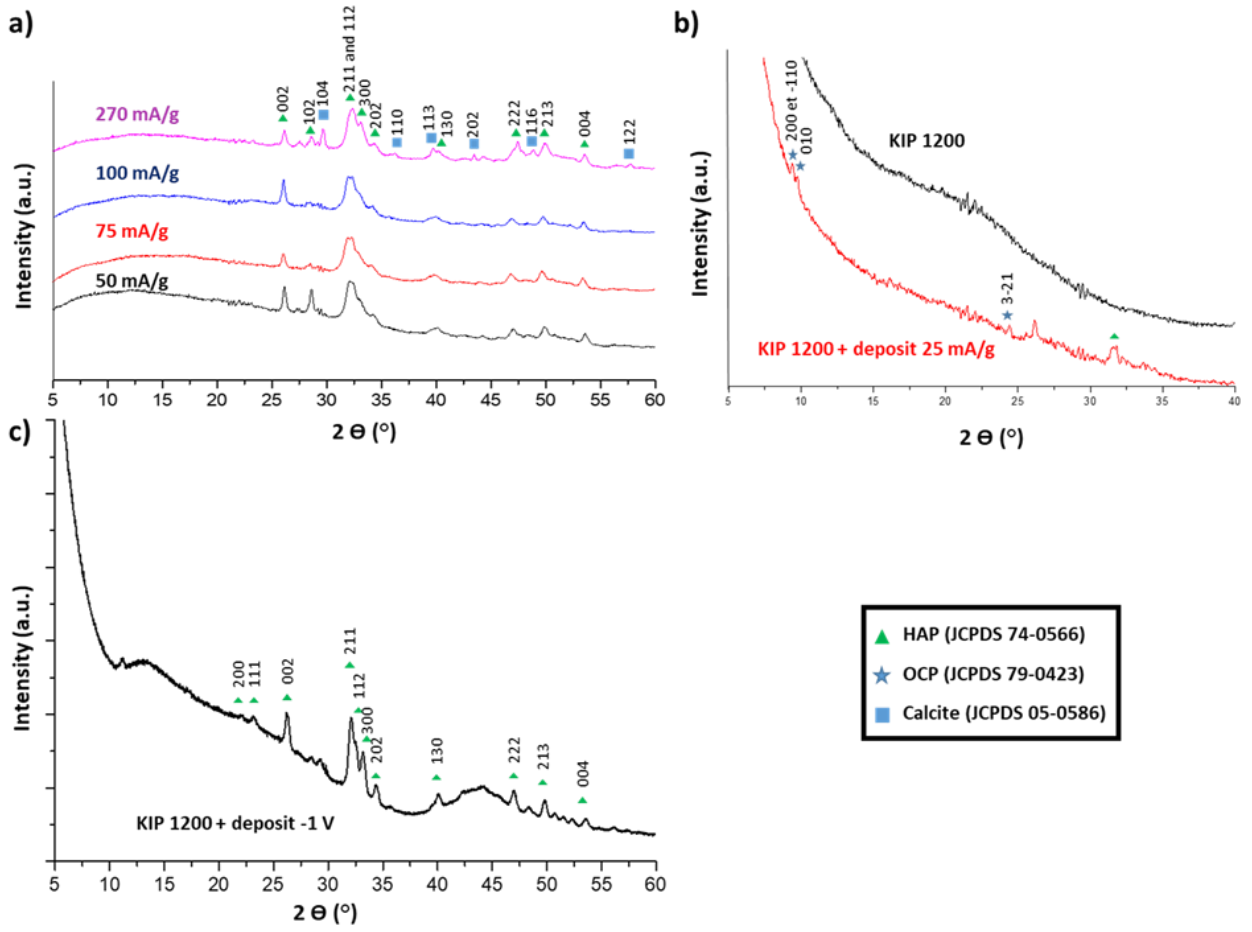

Fig. 8. XRD diffractograms of coatings synthesized at different cathodic polarizations: a) from 50 up to 270 mA/g; powder analysis, b) 25 mA/g; ACC/CaP material analysis, compared with ACC material without coating and c) -1 V constant potential; material analysis (λK_α Cu = 0.154056 nm). **(2-column fitting image + color)**

3.6. Chemical composition of CaP coatings

To further characterize the CaP phases formed during the sono-electrodeposition process, FTIR spectra were recorded. Four main absorption domains are observed in the FTIR spectra (Fig. 9 (a)):

- in the 450-800 cm^{-1} range, the double adsorption band located at 566 and 603 cm^{-1} with the shoulder at 580 cm^{-1} is attributed to the ν_4 bending mode of apatitic PO_4^{3-}. The shoulder observed at 633 cm^{-1} is attributed to the vibration mode of apatitic OH^- (Fig. 9 (b)) [11,61].
- in the 800-1300 cm^{-1} range, the most intense and broad band centred at 1036 cm^{-1} with the shoulder at 1094 cm^{-1} is attributed to the ν_3 bending mode of apatitic PO_4^{3-}. The weak band located at 962 cm^{-1} is attributed to the ν_1 mode *o*f PO_4^{3-} [62]. The very weak absorption band at 873 cm^{-1} can be attributed to HPO_4^{2-} ions and/or CO_3^{2-} ions (Fig. 9 (c)) [63].
- in the 1300-1580 cm^{-1} range, the narrow and weak adsorption band at 1385 cm^{-1} is attributed to a small amount of NO_3^- ions coming from calcium nitrate precursor. Absorption bands between 1400 and 1580 cm^{-1} indicate the existence of structural CO_3^{2-} (Fig. 9 (d)) [11,64].
- in the 1580-4000 cm^{-1} range, broad absorption bands between 1600 and 1800 cm^{-1} and between 2500 and 3700 cm^{-1} are attributed respectively to the occurrence of structural water and adsorbed water in the CaP coating. The weak band observed around 3570 cm^{-1} is attributed to the stretching mode of apatitic OH^- [65].

An expansion of the ν_4 domain corresponding to phosphate ions is shown in Fig. 9 (b). Besides adsorption bands attributed to apatitic phosphate ions (at 566 and 603 cm^{-1} with the

shoulder at 580 cm^{-1}), Mochales *et al.* [66] attributed the broad bands located around 550 and 620 cm^{-1} to non-apatitic HPO_4^{2-} and non-apatitic PO_4^{3-}, respectively.

As shown in Fig. 9 (c), the ν_1 and ν_3 domains attributed to phosphate ions exhibit broad bands characteristic of CDA, except for the FTIR spectrum of 25 mA/g coating which shows several absorption bands at 916 cm^{-1} (P(-OH) stretching mode of HPO_4^{2-}), at 1025, 1038, 1054 and 1077 cm^{-1} (ν_3 stretching mode of PO_4^{3-}), at 1108, 1121 and 1140 cm^{-1} (ν_3 stretching mode of HPO_4^{2-}) and at 1193 cm^{-1} (O-H in-plane vibration mode of HPO_4^{2-}). Amongst these bands, those at 916, 1025 and 1193 cm^{-1} are characteristic of OCP [67].

The ν_3 domain showing bands related to CO_3^{2-} ions is also illustrated in Fig. 9 (d). For all samples, FTIR spectra show broad absorption bands at 1421, 1457 and 1489 cm^{-1} which are attributed to A-type and B-type carbonated HA [11]. The carbonate ions originate from CO_2 dissolved in the electrolyte and the local basic pH close to the carbon scaffold at high current density promotes the formation of carbonate ions, which are incorporated in the apatitic structure during precipitation. This also occurs at low current density and the corresponding FTIR spectra reveal the presence of carbonated CDA beside the OCP phase. For all current densities, it is also possible to assign weak-intensity absorption bands to calcium carbonate phases such as calcite, vaterite or aragonite [68].

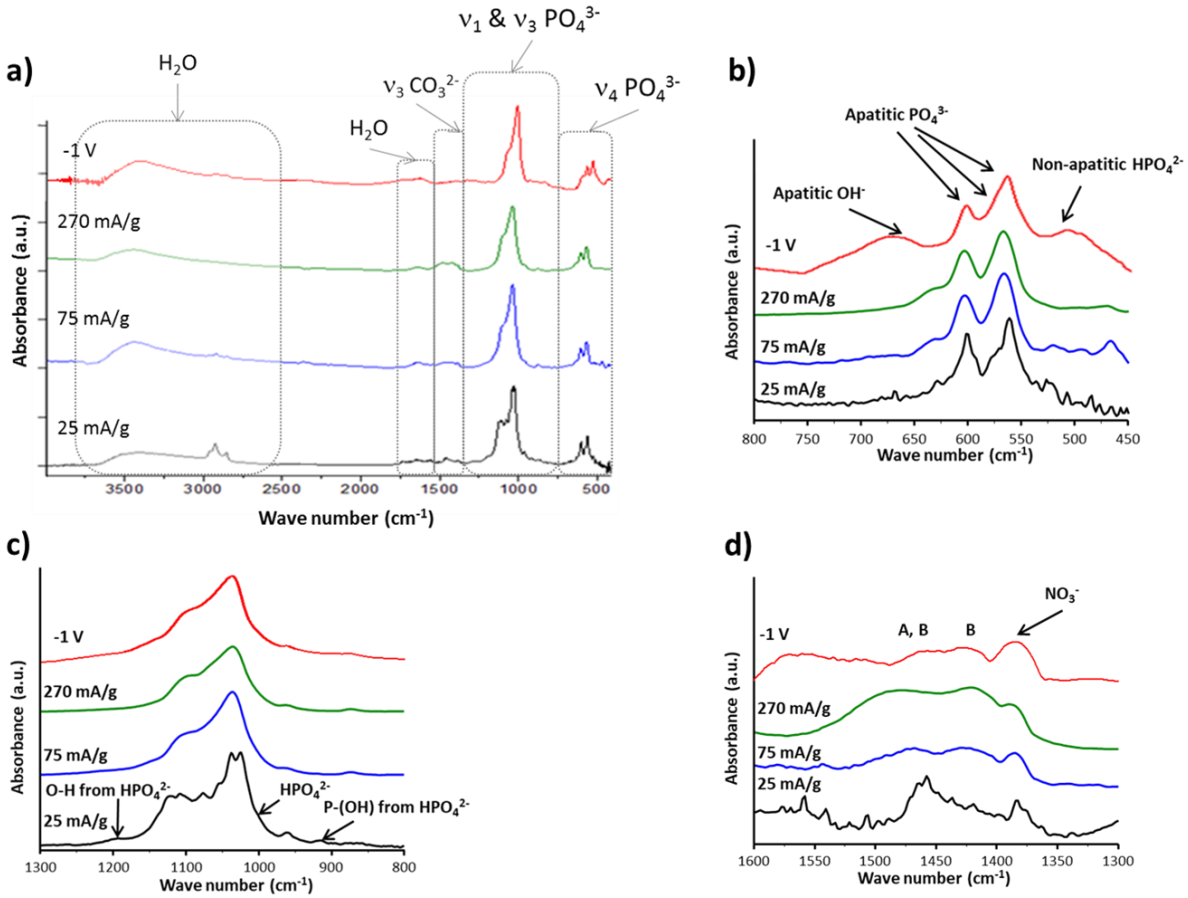

Fig. 9. FTIR spectra of CaP coatings: a) full spectra, b) detail of ν_4 of the PO_3^{4-} region, c) detail of $\nu_1\nu_3$ of the PO_3^{4-} region and d) detail ν_3 of the CO_3^{2-} region. **(2-column fitting image + color)**

3.7. Quantitative structural analysis of CaP coatings

Further structural analyses of the deposited CaP phases were performed using solid-state ^{31}P magic angle spinning (MAS) NMR spectroscopy. As shown in Fig. 10 (a), the quantitative ^{31}P MAS spectra of all samples mainly display an intense peak with an isotropic chemical shift in the range 2.7-2.9 ppm typical of carbonated nanocrystalline HA and CDA [69,70]. The linewidth (FWHM ~ 1.5 ppm) associated to structural disorder is almost the same for all conditions except for the lowest current density for which the quantitative MAS spectrum exhibits a slightly higher signal intensity at lower isotropic chemical shifts (red star). Indeed, cross-polarization (CP) MAS $\{^1H\}$-^{31}P experiments, which enable only the signal of phosphorus atoms in close proximity to

hydrogen ones to be selected, were carried out and revealed the presence of a second resonance located at about 0 ppm which corresponds to the position of the highest-intensity resonance of the OCP CP MAS spectrum (HPO_4 P_5 and P_6 sites) [71,72]. For the coating obtained at 25 mA/g, the ^{31}P MAS spectrum was thus simulated with two subspectra corresponding to the CDA and OCP phases, in agreement with FTIR and XRD results (Fig. 10 (b)). The signal area of these two contributions indicates that roughly 10 and 90 % of the P atoms are involved in the OCP and the carbonated CDA phases, respectively.

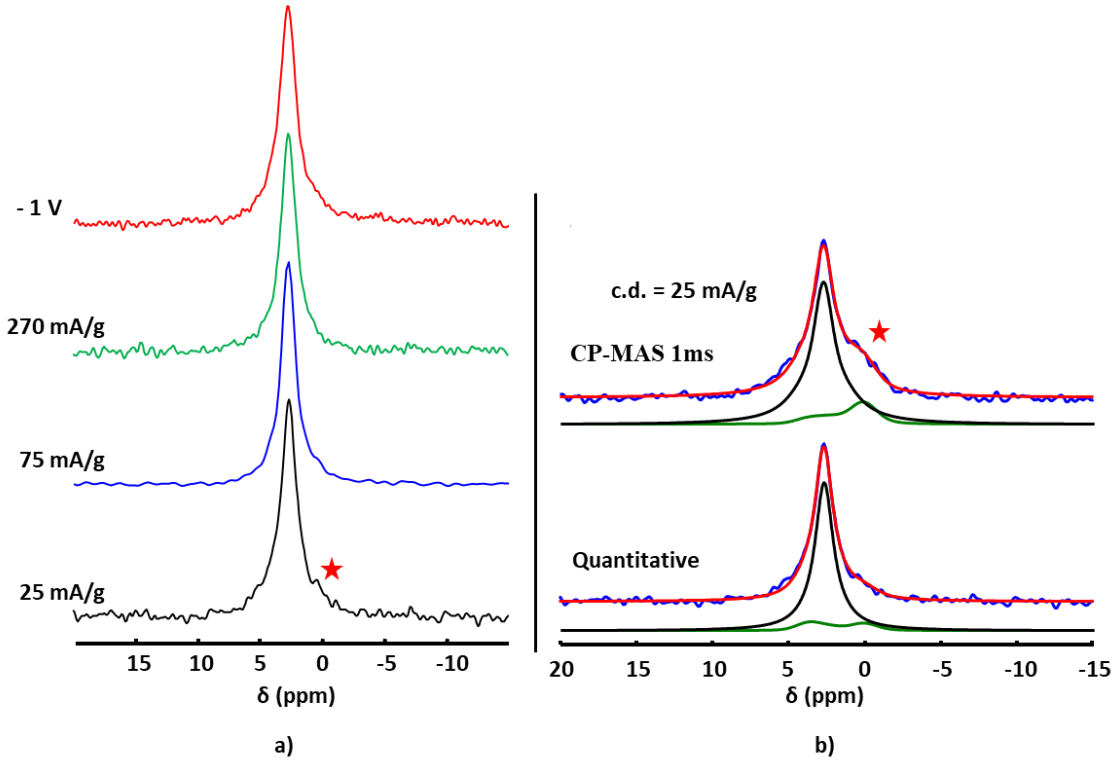

Fig. 10. a) Quantitative ^{31}P MAS NMR spectra of coatings obtained at current densities ranging from 25 to 270 mA/g and at a constant potential (-1 V). b) CP-MAS (contact time of 1 ms) and quantitative MAS NMR spectrum of coating obtained at 25 mA/g. Red: Simulated signal, Black: carbonated CDA contribution, Green: OCP contribution. **(2-column fitting image + color)**

The short-range proximities between P and H atoms (cross-polarization contact time of 1 ms) were deciphered from the 2D ^{31}P-^{1}H heteronuclear correlation (HetCor) MAS NMR spectra, shown in Fig. 11. As expected, these spectra exhibit an intense correlation peak between the ^{31}P

resonance at 2.8-2.9 ppm and the ^{1}H resonance at 0 ppm which are assigned to the phosphate groups and the OH^- hydroxyl ions of the apatitic structure, respectively. In addition, they all show weaker intensity correlation peaks between a wider ^{31}P contribution at almost the same chemical shift (~ 2.8 ppm) and broader ^{1}H signals between 5 and 15 ppm assigned to water molecules and HPO_4 hydrogenophosphate ions. As discussed in previous studies [7,73–75], the former correlation peak is characteristic of the apatitic core of the HA and CDA nanoparticles while the latter ones are associated to the formation of a hydrated disordered surface layer involving HPO_4^{2-} groups. The observation of these features reveals here the strong biomimetic structural character [75,76] of the carbonated HA and CDA phases deposited onto the carbon cloth and ACC surfaces.

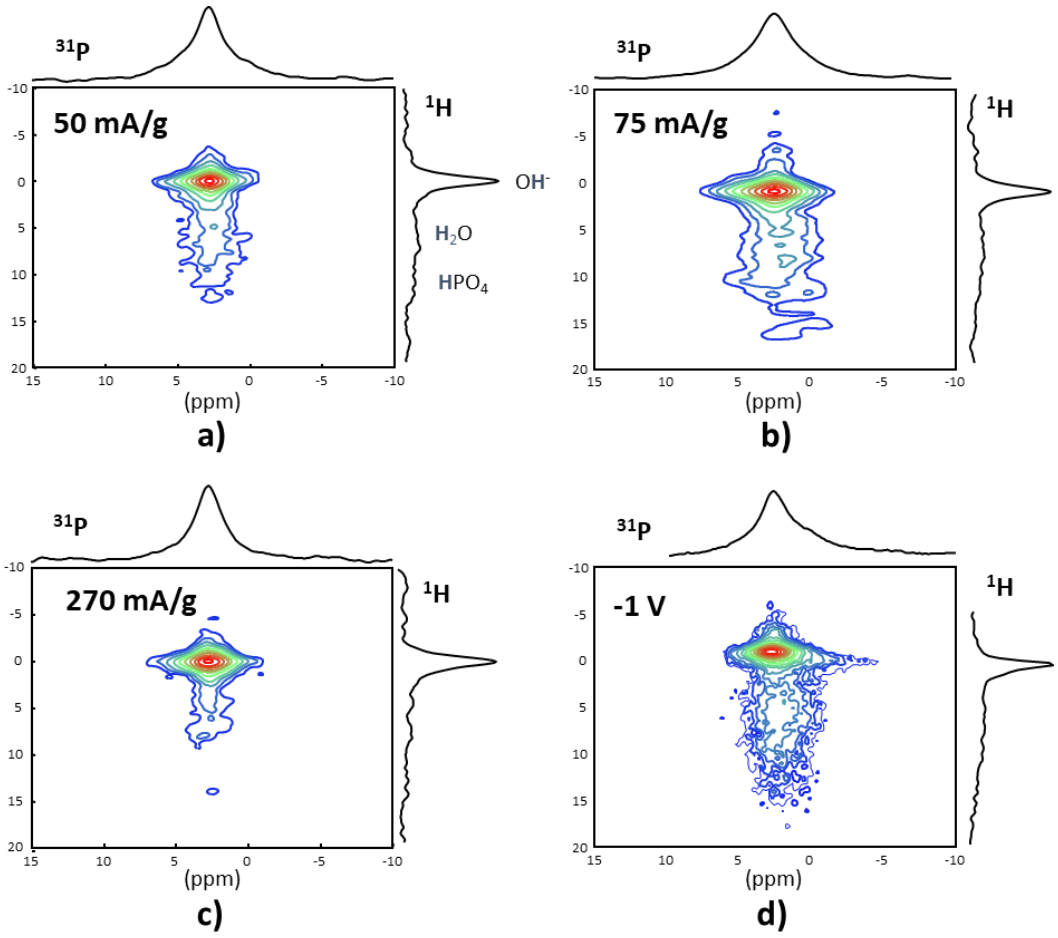

Fig. 11. Two-dimensional {^{1}H}^{31}P HetCor MAS NMR spectra of coatings obtained at a) 25 mA/g, b) 75 mA/g, c) 270 mA/g and -1 V (contact time, tCP = 3 ms). **(2-column fitting image + color)**

3.8. Mechanism of CaP coating formation

The findings described above clearly show that electrochemical parameters make it possible to tune the formation of CaP coatings with different morphologies, compositions, chemical homogeneities, microtextures and structures. These observations can be explained by considering the variations in potential over cathodic polarization time that drive the rate of water electrolysis during the sono-electrodeposition process. These variations for different current densities ranging from 25 to 270 mA/g and at a -1 V constant potential are shown in

Fig. 12. The water reduction potential (-0.94 V) at the initial pH of 4.8 (23°C) is also indicated as a dashed line.

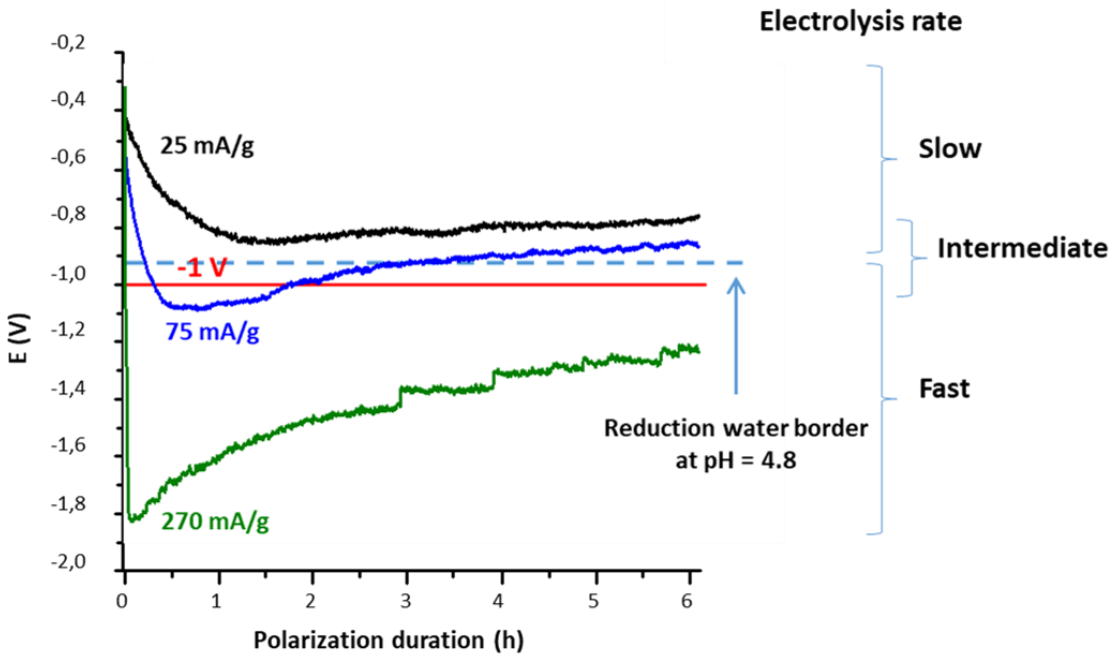

Fig. 12. Variations of potential over time during the sono-electrodeposition at current densities ranging from 25 to 270 mA/g and at -1 V constant potential. **(2-column fitting image + color)**

Depending on the applied current density or potential, three water electrolysis rates can be distinguished. At high current densities (100 to 270 mA/g), the water electrolysis rate is fast since absolute values of measured potentials are greater than the water reduction potential value (-

0.94 V). Consequently, this leads to a significant increase in the local pH close to the carbon cloth and inside its pores, which promotes the precipitation of PO_4^{3-} ions (and HPO_4^{2-} to a much lower extent), to form a nanocrystalline HA phase with a needle-like morphology.

In contrast, water electrolysis occurs much more slowly for low current densities (25 mA/g) since the measured potential never reaches the water reduction value (-0.94 V). This leads to a weak pH increase which allows the existence of HPO_4^{2-} and PO_4^{3-} ions [77] and enables the precipitation of CDA with a plate-like morphology. The observation of OCP to a lower extent suggests that the formation of the CDA phase occurs differently, likely through the precipitation of triclinic OCP with a plate-like morphology which is further transformed into hexagonal CDA as OCP hydrolysis into CDA is easily favored upon a slight increase in local temperature (final bath temperature of 45°C with sonication) and/or pH [78–80]. During the OCP-CDA transition, the weak lattice reorganization occurring due to the loss of water molecules could also allow some carbonate ions to be incorporated in the apatitic structure while keeping a plate-like morphology. Since the OCP hydrolysis rate increases with pH, it also increases with current density.

For intermediate current densities (75 to 100 mA/g), the variations of pH during the process and the crossing of the water electrolysis potential with time, lead to the occurrence of the two morphologies (plate-like and needle-like ones).

For the experiments performed at a -1 V constant potential (corresponding to an applied current density close to 60 mA/g) a better control of water electrolysis is achieved at a slow rate. As a result, the CaP coating is uniform with a well-defined thickness and it consists of a carbonated nanocrystalline CDA phase with plate-like morphology.

4. Conclusion

This study has illustrated the versatility of the sono-electrodeposition process for the coating of carbon fibers and ACC with biomimetic calcium phosphate phases and has described the influence of electrochemical parameters on CaP coating characteristics (morphology, microtexture, chemical composition and structure). It is shown that the use of a constant potential near the water electrolysis potential enables a uniform and homogeneous CaP coating to be obtained. The coating consists of a carbonated calcium-deficient hydroxyapatite (CDA) phase, where the nanocrystalline particles exhibit a plate-like microtexture and are composed of an ordered apatitic core surrounded by a hydrated and disordered surface layer.

Acknowledgements

This work was supported by the FP7-IRSES European program "ABREM" 2012–2015, the Region Centre-Val de Loire projects "MatBioReOs" 2014–2017 and "MatCCaPBio" 2018-2020. The authors are grateful to A. Richard for the SEM images (CME - Univ. Orléans, France**)**.

References

[1] R.Z. Legeros, Calcium Phosphate Materials in Restorative Dentistry: a Review, Adv. Dent. Res. 2 (1988) 164–180. https://doi.org/10.1177/08959374880020011101.

[2] K. de Groot, Clinical applications of calcium phosphate biomaterials: A review, Ceram. Int. 19 (1993) 363–366. https://doi.org/10.1016/0272-8842(93)90050-2.

[3] S.V. Dorozhkin, Calcium orthophosphate bioceramics, Ceram. Int. 41 (2015) 13913–13966. https://doi.org/10.1016/j.ceramint.2015.08.004.

[4] R.A. Surmenev, M.A. Surmeneva, A critical review of decades of research on calcium phosphate–based coatings: How far are we from their widespread clinical application?, Curr. Opin. Biomed. Eng. 10 (2019) 35–44. https://doi.org/10.1016/j.cobme.2019.02.003.

[5] M.P. Ginebra, T. Traykova, J.A. Planell, Calcium phosphate cements as bone drug delivery systems: A review, J. Controlled Release. 113 (2006) 102–110. https://doi.org/10.1016/j.jconrel.2006.04.007.

[6] J. Zhang, W. Liu, V. Schnitzler, F. Tancret, J.-M. Bouler, Calcium phosphate cements for bone substitution: Chemistry, handling and mechanical properties, Acta Biomater. 10 (2014) 1035–1049. https://doi.org/10.1016/j.actbio.2013.11.001.

[7] C. Mellier, F. Fayon, F. Boukhechba, E. Verron, M. LeFerrec, G. Montavon, J. Lesoeur, V. Schnitzler, D. Massiot, P. Janvier, O. Gauthier, J.-M. Bouler, B. Bujoli, Design and properties of novel gallium-doped injectable apatitic cements, Acta Biomater. 24 (2015) 322–332. https://doi.org/10.1016/j.actbio.2015.05.027.

[8] U. Heise, J.F. Osborn, F. Duwe, Hydroxyapatite ceramic as a bone substitute, Int. Orthop. 14 (1990). https://doi.org/10.1007/BF00178768.

[9] M. Parent, A. Magnaudeix, S. Delebassée, E. Sarre, E. Champion, M. Viana Trecant, C. Damia, Hydroxyapatite microporous bioceramics as vancomycin reservoir: Antibacterial efficiency and biocompatibility investigation, J. Biomater. Appl. 31 (2016) 488–498. https://doi.org/10.1177/0885328216653108.

[10] C. Damia, D. Marchat, C. Lemoine, N. Douard, V. Chaleix, V. Sol, N. Larochette, D. Logeart-Avramoglou, J. Brie, E. Champion, Functionalization of phosphocalcic bioceramics for bone repair applications, Mater. Sci. Eng. C. 95 (2019) 343–354. https://doi.org/10.1016/j.msec.2018.01.008.

[11] C. Rey, C. Combes, C. Drouet, H. Sfihi, A. Barroug, Physico-chemical properties of nanocrystalline apatites: Implications for biominerals and biomaterials, Mater. Sci. Eng. C. 27 (2007) 198–205. https://doi.org/10.1016/j.msec.2006.05.015.

[12] D. Grossin, S. Rollin-Martinet, C. Estournès, F. Rossignol, E. Champion, C. Combes, C. Rey, C. Geoffroy, C. Drouet, Biomimetic apatite sintered at very low temperature by spark plasma sintering: Physico-chemistry and microstructure aspects, Acta Biomater. 6 (2010) 577–585. https://doi.org/10.1016/j.actbio.2009.08.021.

[13] T. Kobayashi, K. Gyo, T. Shinohara, N. Yanagihara, Ossicular reconstruction using hydroxyapatite prostheses with interposed cartilage, Am. J. Otolaryngol. 23 (2002) 222–227. https://doi.org/10.1053/ajot.2002.124191.

[14] M. Fricia, M. Passanisi, F. Salamanna, A. Parrilli, G. Giavaresi, M. Fini, Osteointegration in Custom-made Porous Hydroxyapatite Cranial Implants: From Reconstructive Surgery to Regenerative Medicine, World Neurosurg. 84 (2015) 591.e11-591.e16. https://doi.org/10.1016/j.wneu.2015.03.027.

[15] Y. Qing, J. Yi, W. Xiao–yan, Z. Ke–fei, Inflammatory responses to Hydroxyapatite implants in middle ear in rats, J. Otol. 3 (2008) 24–28. https://doi.org/10.1016/S1672-2930(08)50004-3.

[16] L. de Gabory, R. Bareille, D. Stoll, L. Bordenave, J.-C. Fricain, Biphasic calcium phosphate to repair nasal septum: The first in vitro and in vivo study, Acta Biomater. 6 (2010) 909–919. https://doi.org/10.1016/j.actbio.2009.08.018.

[17] L. Yang, S. Jian–jun, Infection associated with hydroxyapatite prosthesis and related factors, J. Otol. 5 (2010) 24–29. https://doi.org/10.1016/S1672-2930(10)50005-9.

[18] S.V. Dorozhkin, Biphasic, triphasic and multiphasic calcium orthophosphates, Acta Biomater. 8 (2012) 963–977. https://doi.org/10.1016/j.actbio.2011.09.003.

[19] J.H. Lee, M.Y. Ryu, H.-R. Baek, K.M. Lee, J.-H. Seo, H.-K. Lee, Fabrication and Evaluation of Porous Beta-Tricalcium Phosphate/Hydroxyapatite (60/40) Composite as a Bone Graft Extender Using Rat Calvarial Bone Defect Model, Sci. World J. 2013 (2013) 1–9. https://doi.org/10.1155/2013/481789.

[20] D.E. Wagner, A.D. Jones, H. Zhou, S.B. Bhaduri, Cytocompatibility evaluation of microwave sintered biphasic calcium phosphate scaffolds synthesized using pH control, Mater. Sci. Eng. C. 33 (2013) 1710–1719. https://doi.org/10.1016/j.msec.2012.12.084.

[21] M. Canillas, P. Pena, A.H. de Aza, M.A. Rodríguez, Calcium phosphates for biomedical applications, Bol. Soc. Esp. Cerámica Vidr. 56 (2017) 91–112. https://doi.org/10.1016/j.bsecv.2017.05.001.

[22] Z.H. Pan, H.P. Cai, P.P. Jiang, Q.Y. Fan, Properties of a Calcium Phosphate Cement Synergistically Reinforced by Chitosan Fiber and Gelatin, J. Polym. Res. 13 (2006) 323–327. https://doi.org/10.1007/s10965-006-9041-2.

[23] Y.S. Pek, S. Gao, M.S.M. Arshad, K.-J. Leck, J.Y. Ying, Porous collagen-apatite nanocomposite foams as bone regeneration scaffolds, Biomaterials. 29 (2008) 4300–4305. https://doi.org/10.1016/j.biomaterials.2008.07.030.

[24] Y. Wang, T. Azaïs, M. Robin, A. Vallée, C. Catania, P. Legriel, G. Pehau-Arnaudet, F. Babonneau, M.-M. Giraud-Guille, N. Nassif, The predominant role of collagen in the nucleation, growth, structure and orientation of bone apatite, Nat. Mater. 11 (2012) 724–733. https://doi.org/10.1038/nmat3362.

[25] X. Zhang, Y. Zhang, X. Zhang, Y. Wang, J. Wang, M. Lu, H. Li, Mechanical properties and cytocompatibility of carbon fibre reinforced nano-hydroxyapatite/polyamide66 ternary biocomposite, J. Mech. Behav. Biomed. Mater. 42 (2015) 267–273. https://doi.org/10.1016/j.jmbbm.2014.11.027.

[26] A. Dorner-Reisel, K. Berroth, R. Neubauer, K. Nestler, G. Marx, M. Scislo, E. Müller, A. Slosarcyk, Unreinforced and carbon fibre reinforced hydroxyapatite: resistance against microabrasion, J. Eur. Ceram. Soc. 24 (2004) 2131–2139. https://doi.org/10.1016/S0955-2219(03)00373-X.

[27] A. Ślósarczyk, M. Klisch, M. Błażewicz, J. Piekarczyk, L. Stobierski, A. Rapacz-Kmita, Hot pressed hydroxyapatite–carbon fibre composites, J. Eur. Ceram. Soc. 20 (2000) 1397–1402. https://doi.org/10.1016/S0955-2219(00)00014-5.

[28] R.F. Banglmaier, E.A. Sander, P.J. VandeVord, Induction and quantification of collagen fiber alignment in a three-dimensional hydroxyapatite–collagen composite scaffold, Acta Biomater. 17 (2015) 26–35. https://doi.org/10.1016/j.actbio.2015.01.033.

[29] R.J. Kane, H.E. Weiss-Bilka, M.J. Meagher, Y. Liu, J.A. Gargac, G.L. Niebur, D.R. Wagner, R.K. Roeder, Hydroxyapatite reinforced collagen scaffolds with improved architecture and mechanical properties, Acta Biomater. 17 (2015) 16–25. https://doi.org/10.1016/j.actbio.2015.01.031.

[30] J. Wang, C. Liu, Biomimetic Collagen/Hydroxyapatite Composite Scaffolds: Fabrication and Characterizations, J. Bionic Eng. 11 (2014) 600–609. https://doi.org/10.1016/S1672-6529(14)60071-8.

[31] X. Wang, X. Zhao, L. Zhang, W. Wang, J. Zhang, F. He, J. Yang, Design and fabrication of carbon fibers with needle-like nano-HA coating to reinforce granular nano-HA composites, Mater. Sci. Eng. C. 77 (2017) 765–771. https://doi.org/10.1016/j.msec.2017.03.307.

[32] P. Kasten, J. Vogel, R. Luginbühl, P. Niemeyer, M. Tonak, H. Lorenz, L. Helbig, S. Weiss, J. Fellenberg, A. Leo, H.-G. Simank, W. Richter, Ectopic bone formation associated with mesenchymal stem cells in a resorbable calcium deficient hydroxyapatite carrier, Biomaterials. 26 (2005) 5879–5889. https://doi.org/10.1016/j.biomaterials.2005.03.001.

[33] S. Hutchens, R. Benson, B. Evans, H. Oneill, C. Rawn, Biomimetic synthesis of calcium-deficient hydroxyapatite in a natural hydrogel, Biomaterials. 27 (2006) 4661–4670. https://doi.org/10.1016/j.biomaterials.2006.04.032.

[34] J. Gustavsson, M.P. Ginebra, E. Engel, J. Planell, Ion reactivity of calcium-deficient hydroxyapatite in standard cell culture media, Acta Biomater. 7 (2011) 4242–4252. https://doi.org/10.1016/j.actbio.2011.07.016.

[35] M. Røkkum, A. Reigstad, Total hip replacement with an entirely hydroxyapatite-coated prosthesis: 5 years' follow-up of 94 consecutive hips, J. Arthroplasty. 14 (1999) 689–700. https://doi.org/10.1016/S0883-5403(99)90224-3.

[36] A. Rogers, R. Kulkarni, E.M. Downes, The ABG hydroxyapatite-coated hip prosthesis: One hundred consecutive operations with average 6-year follow-up1, J. Arthroplasty. 18 (2003) 619–625. https://doi.org/10.1016/S0883-5403(03)00208-0.

[37] E. Chassot, J.L. Irigaray, S. Terver, G. Vanneuville, Contamination by metallic elements released from joint prostheses, Med. Eng. Phys. 26 (2004) 193–199. https://doi.org/10.1016/j.medengphy.2003.10.008.

[38] C.A. Oliveira, I.S. Candelária, P.B. Oliveira, A. Figueiredo, F. Caseiro-Alves, Metallosis: A diagnosis not only in patients with metal-on-metal prostheses, Eur. J. Radiol. Open. 2 (2015) 3–6. https://doi.org/10.1016/j.ejro.2014.11.001.

[39] Y. Yan, A. Neville, D. Dowson, S. Williams, J. Fisher, Effect of metallic nanoparticles on the biotribocorrosion behaviour of Metal-on-Metal hip prostheses, 17th Int. Conf. Wear Mater. 267 (2009) 683–688. https://doi.org/10.1016/j.wear.2008.12.110.

[40] N. Eliaz, T.M. Sridhar, Electrocrystallization of Hydroxyapatite and Its Dependence on Solution Conditions, Cryst. Growth Des. 8 (2008) 3965–3977. https://doi.org/10.1021/cg800016h.

[41] P. Choudhury, D.C. Agrawal, Sol–gel derived hydroxyapatite coatings on titanium substrates, Surf. Coat. Technol. 206 (2011) 360–365. https://doi.org/10.1016/j.surfcoat.2011.07.031.

[42] C.J. Tredwin, G. Georgiou, H.-W. Kim, J.C. Knowles, Hydroxyapatite, fluor-hydroxyapatite and fluorapatite produced via the sol–gel method: Bonding to titanium and scanning electron microscopy, Dent. Mater. 29 (2013) 521–529. https://doi.org/10.1016/j.dental.2013.02.002.

[43] H. Khandelwal, G. Singh, K. Agrawal, S. Prakash, R.D. Agarwal, Characterization of hydroxyapatite coating by pulse laser deposition technique on stainless steel 316 L by varying laser energy, Appl. Surf. Sci. 265 (2013) 30–35. https://doi.org/10.1016/j.apsusc.2012.10.072.

[44] E.N. Bolbasov, I.N. Lapin, V.A. Svetlichnyi, Y.D. Lenivtseva, A. Malashicheva, Y. Malashichev, A.S. Golovkin, Y.G. Anissimov, S.I. Tverdokhlebov, The formation of calcium phosphate coatings by pulse laser deposition on the surface of polymeric ferroelectric, Appl. Surf. Sci. 349 (2015) 420–429. https://doi.org/10.1016/j.apsusc.2015.05.025.

[45] L.E. Macaskie, P. Yong, M. Paterson-Beedle, A.C. Thackray, P.M. Marquis, R.L. Sammons, K.P. Nott, L.D. Hall, A novel non line-of-sight method for coating hydroxyapatite onto the surfaces of support materials by biomineralization, J. Biotechnol. 118 (2005) 187–200. https://doi.org/10.1016/j.jbiotec.2005.03.006.

[46] D. Gopi, J. Indira, L. Kavitha, A comparative study on the direct and pulsed current electrodeposition of hydroxyapatite coatings on surgical grade stainless steel, Surf. Coat. Technol. 206 (2012) 2859–2869. https://doi.org/10.1016/j.surfcoat.2011.12.011.

[47] N. Dumelie, H. Benhayoune, D. Richard, D. Laurent-Maquin, G. Balossier, In vitro precipitation of electrodeposited calcium-deficient hydroxyapatite coatings on Ti6Al4V substrate, Mater. Charact. 59 (2008) 129–133. https://doi.org/10.1016/j.matchar.2006.11.030.

[48] N. Eliaz, M. Eliyahu, Electrochemical processes of nucleation and growth of hydroxyapatite on titanium supported by real-time electrochemical atomic force microscopy, J. Biomed. Mater. Res. A. 80A (2007) 621–634. https://doi.org/10.1002/jbm.a.30944.

[49] N. Metoki, D. Mandler, N. Eliaz, Effect of Decorating Titanium with Different Self-Assembled Monolayers on the Electrodeposition of Calcium Phosphate, Cryst. Growth Des. 16 (2016) 2756–2764. https://doi.org/10.1021/acs.cgd.6b00057.

[50] E. Vidal, J. Buxadera-Palomero, C. Pierre, J.M. Manero, M.-P. Ginebra, S. Cazalbou, C. Combes, E. Rupérez, D. Rodríguez, Single-step pulsed electrodeposition of calcium phosphate coatings on titanium for drug delivery, Surf. Coat. Technol. 358 (2019) 266–275. https://doi.org/10.1016/j.surfcoat.2018.11.037.

[51] R. Drevet, J. Fauré, S. Sayen, M. Marle-Spiess, H. El Btaouri, H. Benhayoune, Electrodeposition of biphasic calcium phosphate coatings with improved dissolution properties, Mater. Chem. Phys. 236 (2019) 121797. https://doi.org/10.1016/j.matchemphys.2019.121797.

[52] R. Walter, M. Bobby Kannan, Y. He, A. Sandham, Influence of the cathodic activity of magnesium alloys on the electrochemical deposition of calcium phosphate, Mater. Lett. 130 (2014) 184–187. https://doi.org/10.1016/j.matlet.2014.05.125.

[53] N. Monasterio, J.L. Ledesma, I. Aranguiz, A. Garcia-Romero, E. Zuza, Analysis of electrodeposition processes to obtain calcium phosphate layer on AZ31 alloy, Surf. Coat. Technol. 319 (2017) 12–22. https://doi.org/10.1016/j.surfcoat.2017.03.060.

[54] H. Hong-mei, S.V. Mikhalovsky, G.J. Phillips, A.W. Lloyd, Calcium phosphate sonoelectrodeposition on carbon fabrics and its effect on osteoblast cell viability in vitro, New Carbon Mater. (2007) 5.

[55] M. Wu, Q. Wang, X. Liu, H. Liu, Biomimetic synthesis and characterization of carbon nanofiber/hydroxyapatite composite scaffolds, Carbon. 51 (2013) 335–345. https://doi.org/10.1016/j.carbon.2012.08.061.

[56] X. Wang, X. Zhao, W. Wang, J. Zhang, L. Zhang, F. He, J. Yang, Controllable preparation of a nano-hydroxyapatite coating on carbon fibers by electrochemical deposition and chemical treatment, Mater. Sci. Eng. C. 63 (2016) 96–105. https://doi.org/10.1016/j.msec.2016.02.058.

[57] X. Zhao, X. Wang, H. Xin, L. Zhang, J. Yang, G. Jiang, Controllable preparation of SiC coating protecting carbon fiber from oxidation damage during sintering process and SiC coated carbon fiber reinforced hydroxyapatite composites, Appl. Surf. Sci. 450 (2018) 265–273. https://doi.org/10.1016/j.apsusc.2018.04.164.

[58] H. Han, S.V. Mikhalovsky, G.J. Phillips, A.W. Lloyd, Calcium phosphate sonoelectrodeposition on carbon fabrics and its effect on osteoblast cell viability in vitro, New Carbon Mater. 22 (2007) 121–125. https://doi.org/10.1016/S1872-5805(07)60012-2.

[59] H. Han, G.J. Phillips, S.V. Mikhalovsky, A.W. Lloyd, In vitro cytotoxicity assessment of carbon fabric coated with calcium phosphate, New Carbon Mater. 23 (2008) 139–143. https://doi.org/10.1016/S1872-5805(08)60017-7.

[60] H.M. Han, G.J. Phillips, S.V. Mikhalovsky, S. FitzGerald, A.W. Lloyd, Sonoelectrochemical deposition of calcium phosphate coatings on carbon materials—effect of electrolyte concentration, J. Mater. Sci. Mater. Med. 19 (2008) 2845–2850. https://doi.org/10.1007/s10856-008-3411-8.

[61] N. Vandecandelaere, C. Rey, C. Drouet, Biomimetic apatite-based biomaterials: on the critical impact of synthesis and post-synthesis parameters, J. Mater. Sci. Mater. Med. 23 (2012) 2593–2606. https://doi.org/10.1007/s10856-012-4719-y.

[62] C. Rey, M. Shimizu, B. Collins, M.J. Glimcher, Resolution-enhanced fourier transform infrared spectroscopy study of the environment of phosphate ion in the early deposits of a solid phase of calcium phosphate in bone and enamel and their evolution with age: 2. Investigations in thev 3 PO4 domain, Calcif. Tissue Int. 49 (1991) 383–388. https://doi.org/10.1007/BF02555847.

[63] C. Rey, C. Combes, C. Drouet, D. Grossin, Bioactive Ceramics: Physical Chemistry, in: Compr. Biomater., Elsevier, 2011: pp. 187–221. https://doi.org/10.1016/B978-0-08-055294-1.00178-1.

[64] C. Rey, B. Collins, T. Goehl, I.R. Dickson, M.J. Glimcher, The carbonate environment in bone mineral: A resolution-enhanced fourier transform infrared spectroscopy study, Calcif. Tissue Int. 45 (1989) 157–164. https://doi.org/10.1007/BF02556059.

[65] C.G. Weber, M. Mueller, N. Vandecandelaere, I. Trick, A. Burger-Kentischer, T. Maucher, C. Drouet, Enzyme-functionalized biomimetic apatites: concept and perspectives in view of innovative medical approaches, J. Mater. Sci. Mater. Med. 25 (2014) 595–606. https://doi.org/10.1007/s10856-013-5097-9.

[66] C. Mochales, R.M. Wilson, S.E.P. Dowker, M.-P. Ginebra, Dry mechanosynthesis of nanocrystalline calcium deficient hydroxyapatite: Structural characterisation, J. Alloys Compd. 509 (2011) 7389–7394. https://doi.org/10.1016/j.jallcom.2011.04.033.

[67] B.O. Fowler, E.C. Moreno, W.E. Brown, Infra-red spectra of hydroxyapatite, octacalcium phosphate and pyrolysed octacalcium phosphate, Arch. Oral Biol. 11 (1966) 477–492. https://doi.org/10.1016/0003-9969(66)90154-3.

[68] H. Maeda, T. Kasuga, M. Nogami, Apatite formation on titania–vaterite powders in simulated body fluid, J. Eur. Ceram. Soc. 24 (2004) 2125–2130. https://doi.org/10.1016/S0955-2219(03)00327-3.

[69] R.N. Panda, M.F. Hsieh, R.J. Chung, T.S. Chin, FTIR, XRD, SEM and solid state NMR investigations of carbonate-containing hydroxyapatite nano-particles synthesized by hydroxide-gel technique, J. Phys. Chem. Solids. 64 (2003) 193–199. https://doi.org/10.1016/S0022-3697(02)00257-3.

[70] W.P. Aue, A.H. Roufosse, M.J. Glimcher, R.G. Griffin, Solid-state phosphorus-31 nuclear magnetic resonance studies of synthetic solid phases of calcium phosphate: potential models of bone mineral, Biochemistry. 23 (1984) 6110–6114.

[71] Y.-H. Tseng, J. Zhan, K.S.K. Lin, C.-Y. Mou, J.C.C. Chan, High resolution 31P NMR study of octacalcium phosphate, Solid State Nucl. Magn. Reson. 26 (2004) 99–104. https://doi.org/10.1016/j.ssnmr.2004.06.002.

[72] E. Davies, M.J. Duer, S.E. Ashbrook, J.M. Griffin, Applications of NMR Crystallography to Problems in Biomineralization: Refinement of the Crystal Structure and ^{31} P Solid-State NMR Spectral Assignment of Octacalcium Phosphate, J. Am. Chem. Soc. 134 (2012) 12508–12515. https://doi.org/10.1021/ja3017544.

[73] H. Roussière, G. Montavon, S. Laïb, P. Janvier, B. Alonso, F. Fayon, M. Petit, D. Massiot, J.-M. Bouler, B. Bujoli, Hybrid materials applied to biotechnologies: coating of calcium phosphates for the design of implants active against bone resorption disorders, J. Mater. Chem. 15 (2005) 3869. https://doi.org/10.1039/b503680a.

[74] C. Jäger, T. Welzel, W. Meyer-Zaika, M. Epple, A solid-state NMR investigation of the structure of nanocrystalline hydroxyapatite, Magn. Reson. Chem. 44 (2006) 573–580. https://doi.org/10.1002/mrc.1774.

[75] Y. Wang, S. Von Euw, F.M. Fernandes, S. Cassaignon, M. Selmane, G. Laurent, G. Pehau-Arnaudet, C. Coelho, L. Bonhomme-Coury, M.-M. Giraud-Guille, F. Babonneau, T. Azaïs, N. Nassif, Water-mediated structuring of bone apatite, Nat. Mater. 12 (2013) 1144–1153. https://doi.org/10.1038/nmat3787.

[76] S. Von Euw, W. Ajili, T.-H.-C. Chan-Chang, A. Delices, G. Laurent, F. Babonneau, N. Nassif, T. Azaïs, Amorphous surface layer versus transient amorphous precursor phase in bone – A case study investigated by solid-state NMR spectroscopy, Acta Biomater. 59 (2017) 351–360. https://doi.org/10.1016/j.actbio.2017.06.040.

[77] E.A. Abdel-Aal, D. Dietrich, S. Steinhaeuser, B. Wielage, Electrocrystallization of nanocrystallite calcium phosphate coatings on titanium substrate at different current densities, Surf. Coat. Technol. 202 (2008) 5895–5900. https://doi.org/10.1016/j.surfcoat.2008.06.139.

[78] W.E. BROWN, J.P. SMITH, J.R. LEHR, A.W. FRAZIER, Octacalcium Phosphate and Hydroxyapatite: Crystallographic and Chemical Relations between Octacalcium Phosphate and Hydroxyapatite, Nature. 196 (1962) 1050–1055. https://doi.org/10.1038/1961050a0.

[79] S. Graham, P.W. Brown, Reactions of octacalcium phosphate to form hydroxyapatite, J. Cryst. Growth. 165 (1996) 106–115. https://doi.org/10.1016/0022-0248(95)00994-9.

[80] M.J. Arellano-Jiménez, R. García-García, J. Reyes-Gasga, Synthesis and hydrolysis of octacalcium phosphate and its characterization by electron microscopy and X-ray diffraction, J. Phys. Chem. Solids. 70 (2009) 390–395. https://doi.org/10.1016/j.jpcs.2008.11.001.